Characterization of initial intergranular oxidation processes in alloy 600 at a sub-nanometer scale

S.Y. Persaud[a,*], B. Langelier[b], A. Korinek[b], S. Ramamurthy[c], G.A. Botton[b], R.C. Newman[d,*]

[a] Department of Mechanical and Materials Engineering, Queen's University, Nicol Hall, 60 Union Street W, Kingston, ON, K7L 2N8, Canada
[b] Department of Materials Science and Engineering, and Canadian Centre for Electron Microscopy, McMaster University, 1280 Main Street West, Hamilton, ON, L8S 4M1, Canada
[c] Surface Science Western, University of Western Ontario, 999 Collip Circle, London, ON, N6G 0J3, Canada
[d] Department of Chemical Engineering and Applied Chemistry, University of Toronto, 200 College Street, Toronto, ON, M5S 3E5, Canada

ARTICLE INFO

ABSTRACT

Intergranular oxidation in Alloy 600 exposed to 480 °C hydrogenated steam was examined at the nano-scale level with analytical electron microscopy and atom probe tomography. The fundamental processes of minor element oxidation and diffusion-induced grain boundary migration (DIGM) were explored. Intergranular oxidation was observed, with Ti and Al oxidation preceding Cr oxidation. Extensive DIGM is observed, with concentrations of minor elements far exceeding bulk values. Calculations are performed which support that the mechanism of DIGM causes large-scale segregation of minor elements. Also, discrete oxide particles ahead of the oxide front provide evidence for classical intergranular internal oxidation at temperatures below 500 °C.

1. Introduction

Alloy 600 (Ni-16Cr-9Fe) is a Ni alloy that was originally chosen for steam generator tubing and other components on the primary side of nuclear power plants due to its resistance to chloride stress corrosion cracking (SCC). However, the alloy was found to be highly susceptible to SCC in the reducing conditions of primary water (PWSCC) and was subsequently replaced in many nuclear power plants. The temperature of primary water ranges from 280 °C to 320 °C in Canada deuterium uranium (CANDU) reactors and can reach up to 340 °C in pressurized water reactors (PWR). Lithium hydroxide and boric acid are added to regulate pH, depending on the reactor design. In addition, hydrogen is added which reduces the potential of primary water into the range of the Ni/NiO electrode potential. PWSCC growth rate in Alloy 600 has been reported to peak in the vicinity of the Ni/NiO equilibrium potential [1–5], suggesting the possibility of internal oxidation. Scott and Le Calvar were first to suggest that PWSCC in Alloy 600 occurred due to internal oxidation [6], a phenomenon often observed in Ni superalloys at much higher temperatures [7–14]. Internal oxidation occurs in binary or ternary alloys which contain a noble solvent element, such as Ni, and a lower concentration of a more reactive solute element, such as Cr. In conditions where the oxygen partial pressure is in the vicinity of the dissociation pressure of the noble solvent metal oxide, the reactive element, if below a critical concentration, can oxidize internally rather

than externally [7–9,15–22]; intergranular internal oxidation can result in embrittlement and SCC.

Since the initial proposal of internal oxidation as the mechanism of PWSCC in Alloy 600, several studies have investigated the phenomenon in both 300 °C–360 °C primary water environments [23–29] and 400 °C–500 °C hydrogenated steam [17–19,30–41], a simulated primary water environment. The use of high temperature hydrogenated steam to model primary water conditions was concluded to be valid by Economy et al., who found that the time to 30% IGSCC in Alloy 600 lay on one Arrhenius line over the 300 °C primary water to 400 °C hydrogenated steam range [36]. Also, lattice diffusion is essentially negligible in hydrogenated steam below 500 °C, similar to primary water. Furthermore, experimental observation of intragranular internal oxidation has been demonstrated in Alloy 600 and other Ni alloys extending from 300 °C water to 500 °C hydrogenated steam [15,16,18,29,37,38,40,42–44]; in the latter environment, expulsion of the solvent Ni has been reported, in accordance with classical internal oxidation. The compressive stress generated during internal oxidation results in the noble solvent metal being expelled to the surface, likely diffusing along short-circuit oxide-metal interfaces [40].

Preferential intergranular oxidation of Cr and other minor impurities (e.g. Ti, Al), extending down from the sample surface, has been previously reported in primary water environments and high temperature hydrogenated steam [18,34,37–40]. The high concentration of

* Corresponding authors.
E-mail addresses: suraj.persaud@queensu.ca (S.Y. Persaud), roger.newman@utoronto.ca (R.C. Newman).

Table 1
Composition of Alloy 600 purchased from Rolled Alloys Inc. in wt.% and (at.%).

Ni Bal.	Cr	Fe	Ti	Mn	Al	Cu	Co	Si	Nb	C	S	P
73.8 (71.7)	15.8 (17.3)	9.4 (9.6)	0.31 (0.37)	0.21 (0.22)	0.16 (0.34)	0.16 (0.14)	0.05 (0.05)	0.05 (0.10)	0.03 (0.02)	0.02 (0.09)	0.001 (0.000)	0.005 (0.000)

minor impurity elements at grain boundaries after exposure to representative primary water conditions is surprising given the severely hindered lattice diffusion kinetics, even with short-circuit dislocation and/or oxide-metal interface diffusion. Diffusion-induced grain boundary migration (DIGM) has been noted in Ni alloys after exposure to representative primary water conditions and high temperature hydrogenated steam and has been speculated to influence diffusion kinetics [37,38,41,44–47]. DIGM is movement of grain boundaries caused by the diffusion of reactive solute alloying elements to the grain boundary. For example, in Alloy 600 exposed to reducing steam/water, the diffusion of Al, Ti, and Cr to grain boundaries to form thermodynamically favourable intergranular oxides from adjacent grains acts as a driving force for DIGM. The mobility of the grain boundary accommodates reactive solute element diffusion from the more favourable grain and results in depletion of these solute elements in the volume between the migrated boundary and the original grain boundary plane. DIGM effectively "sweeps" reactive elements to the grain boundary, thereby increasing the overall outward intergranular flux far beyond that expected through conventional grain boundary/lattice diffusion, specifically relevant to conditions where lattice diffusion is essentially negligible. Langelier et al. and Bertali et al. have suggested that this DIGM process and minor element oxidation could play a significant role in intergranular oxidation of Alloy 600, possibly during initial stages, but further work is required to confirm such an effect [37–39,41].

The formation of discrete intergranular internal oxide particles, as originally proposed by Scott [6], has not yet been observed in Alloy 600. As a result, the mechanism of PWSCC in Alloy 600 has, thus far, been classified as continuous intergranular preferential or selective Cr oxidation embrittlement, which occurs because of conditions being near the Ni/NiO equilibrium electrode potential or oxygen dissociation pressure, analogous to internal oxidation. Intergranular internal oxidation, as originally proposed, may still be possible well ahead of the intergranular oxide front as a precursor to the formation of the continuous preferential intergranular oxide; however, this possibility has not been investigated extensively. In general, the initial processes occurring during intergranular oxidation of Alloy 600 in primary water, possibly minor impurity segregation and/or discrete internal oxide precipitation, are not yet well understood.

The mechanism of PWSCC in Alloy 600 is suggested to be continuous preferential intergranular Cr oxidation, which occurs for similar reasons as internal oxidation observed at much higher temperatures. However, the study of initial oxidation processes at a sub-nanometer scale remains an area of interest, particularly in high temperature hydrogenated steam environments. Under such conditions, no prior work has been undertaken other than the observation of minor impurity oxidation [18,29,37–39,41]. Analytical transmission electron microscopy (TEM) work by Persaud et al. [17,18,41] and Bertali et al. [37–39] has provided insight into intergranular oxidation of Alloy 600 in 480 °C hydrogenated steam, but their analysis was unable to conclusively verify how early-stage oxidation processes occur. Further understanding of the intergranular oxide and related microstructure can be provided by atom probe tomography (APT). APT relies on spatial and elemental measurement of ions that are successively field-evaporated from a small volume of material, with the data able to be reconstructed into a 3D model of that material volume. APT has typically been limited to conductive materials (i.e. metals and alloys), but the implementation of pulsed-laser atom probes has opened up the

technique to studying non-conducting materials, such as oxides [48–52]. This analysis technique couples high spatial and elemental resolution, and offers the ability to study intergranular oxidation at the near atomic-scale. In the current study, APT and TEM are used to examine grain boundary chemistry in Alloy 600, after exposure to 480 °C hydrogenated steam with conditions maintained well below the Ni/NiO equilibrium oxygen dissociation pressure. Analysis using information gathered from a combination of these two high resolution techniques are performed to verify whether DIGM is a plausible explanation for the segregation and formation of minor impurity (i.e. Ti and/or Al) intergranular oxides. Examinations are also conducted well ahead of the continuous preferential intergranular oxide front, which show that formation of discrete internal oxide precipitates is possible in Alloy 600 at 500 °C and below.

2. Experimental methods

2.1. Materials and sample preparation

A 1.3 mm thick Alloy 600 sheet obtained from Rolled Alloys Inc. was used for all exposures; the composition of the material is given in Table 1. Flat coupons were cut from the sheet measuring 1 cm by 1 cm. All coupons were solution annealed (SA) at 1050 °C in high purity Ar gas for one hour and immediately water quenched.

Flat coupons were ground using 400, 800, and 1200 grit paper. Following this, step-wise fine polishing was done using diamond paste (9 μm, 3 μm, and 1 μm) and alumina suspension to a 0.05 μm finish. Samples were ultrasonically cleaned in ethanol and de-ionized water for 10 min each between polishing stages and dried with air. A desiccator was used to preserve samples for a short period until the time of exposure.

The geometry and surface finish chosen for the present study are meant to simplify material conditions to allow for easier study of initial oxidation processes in ideal conditions, not necessarily representative of in-service steam generator tubing. Future work will involve examination of geometry and surface cold work effects on SCC susceptibility, intergranular oxidation, and diffusion of alloying elements.

2.2. Experimental conditions and procedures

Experiments were carried out in an atmospheric pressure reactor at Surface Science Western, London, ON, Canada. The reactor was based on the design in work previously done by Scenini et al. [19]. Samples were exposed to a 480 °C hydrogenated steam environment for 120 h with a pre-determined oxygen partial pressure that set conditions well below the Ni/NiO equilibrium oxygen dissociation pressure (on the Ni-metal side). The oxygen partial pressure was set such that conditions were maintained approximately 30 times below the Ni/NiO equilibrium oxygen dissociation pressure, which prevented Ni oxidation and allowed for a clearer study on the role of minor impurity alloying elements, chromium and oxygen. It should be noted that "reactive elements" described in the present study are minor alloying elements in Alloy 600 that are more reactive than the noble Ni base metal. Hydrogen and water flow rates used to promote the necessary conditions were determined through conventional thermodynamic calculations; detailed calculations can be found in previous work by the authors [17,18].

The chosen experimental conditions are meant to simulate

accelerated primary water conditions (320 °C–360 °C with added hydrogen). In conventional PWR primary water, the electrochemical potential is usually maintained in the vicinity of the Ni/NiO equilibrium, on the Ni-metal side, and SCC is a known possibility under these conditions [1–5]. The 480 °C hydrogenated steam environment in the present study is maintained slightly more reducing to eliminate the possibility of Ni oxidation for easier interpretation of the behavior of minor alloying elements and oxygen. A parabolic relation for crack growth rate versus hydrogen content has been reported in both high temperature water [1–5] and 480 °C hydrogenated steam [33], peaking in the vicinity of the Ni/NiO equilibrium; this further supports the validity of high temperature steam as a simulated primary water environment.

A brief description of the system and experimental procedure is provided here; a process flow diagram with detailed procedures can be found in a previous study by the authors [17,18]. A tube reactor enclosed in a furnace was used for all exposures. Polished samples were placed in the centre of the reactor tube. The furnace is unable to encase the ends of the tube and high temperature tapes were used to heat exposed areas. High purity argon gas was used to deaerate the system prior to starting the hydrogenated steam flow. De-ionized water was pumped into the system using a peristaltic pump. Water and hydrogen were fed into a stainless steel block at 300 °C where water was vaporized and they were mixed prior to entering the reactor. The ratio of steam to hydrogen was controlled such that the oxygen partial pressure was maintained at conditions 30 times below the Ni/NiO equilibrium oxygen dissociation pressure. Upon exit from the reactor, the hydrogenated steam was separated into hydrogen and water by way of a condenser. The hydrogen was combusted using a methane burner in a fume hood while condensed water was collected in a beaker.

2.3. Transmission electron microscopy (TEM)

TEM samples were prepared by performing a standard lift-out procedure using an NVision 40 (Carl Zeiss, Germany) scanning electron microscope (SEM) equipped with a focused ion beam (FIB). Lift-out samples from the oxidized grain boundaries were attached to Cu half-grids using W deposition, and thinned to electron transparency using the Ga ion FIB at successively lower voltages of 30 kV, 10 kV, and 5 kV. Complete details for the lift-out procedure for the grain boundaries in Alloy 600 samples are described in Ref. [18].

Samples were analyzed with scanning transmission electron microscopy (STEM) using a FEI Titan 80–300 (FEI Company, The Netherlands) at an accelerating voltage of 300 kV, and using a high-angle annular dark field (HAADF) detector. Composition analysis was performed using electron energy loss spectroscopy (EELS) and a GIF Tridiem 865 spectrometer (Gatan Inc., USA).

2.4. Atom probe tomography (APT)

APT requires finely-tipped needle-shaped specimens to achieve the field strengths necessary for analysis. A FIB was utilized to prepare samples of such a shape, from the site-specific location of the grain boundaries in Alloy 600. Based on established lift-out techniques for the extraction and sharpening of APT samples (see [53]), first the area of interest (i.e. an oxidized grain boundary) is identified (Fig. 1(a)). The sample targeted for extraction is then protected from the ion beam by depositing a layer of W on the surface. Cuts are made at 60° to the sample surface, along the grain boundary, to cut out a wedge-shaped specimen that is 15–20 μm long (Fig. 1(b)) and triangular in cross-section. This long wedge of material is then extracted using the FIB manipulator (Fig. 1(c)). Smaller sections of the extracted volume, approximately 2–3 μm in length along the long axis of the wedge, are then affixed to Si posts using W deposition, and cut-off from the original long wedge (Fig. 1(d)).

Each small volume, attached to the Si posts, is then sharpened into needles for APT analysis. This procedure involves identifying the region of interest by using a 30 kV Ga ion beam to mill away material along the cross-section of the sample, normal to the grain boundary (Fig. 2(a)). By examining the cross-section of the sample, the oxide penetration down the grain boundary and into the sample can be observed (Fig. 2(b)). The exact location of a feature of interest (i.e. a certain point along the oxidized boundary) is then targeted for APT analysis, and the tip sharpened to that exact location. The sharpening procedure first uses a 30 kV Ga ion beam, run in an annular pattern, top-down along the specimen axis, to produce a small pillar (Fig. 2(c)). Final sharpening then uses a reduced voltage of 10 kV and a relatively defocused beam to minimize damage from the Ga ions and obtain the final tip shape. This last stage of sharpening is continued until the feature of interest (i.e. the grain boundary) is within 100–200 nm of the tip apex (Fig. 2(d)).

A local electrode atom probe (LEAP) 4000X HR (CAMECA Scientific Instruments, Madison, WI) was used for all APT analysis. Acquisition of atom probe data was conducted in ultra-high vacuum ($< 4 \times 10^{-9}$ Pa) with a base sample temperature of approximately 60 K. Field evaporation of the samples was induced using ultraviolet (UV) laser pulses (l = 355 nm, 40–60 pJ, 200 kHz). The UV wavelength range is reported to be effective in optimizing the mass resolving power when performing APT analysis on oxides [49]. A DC voltage of approximately 2–9 kV was applied to the sample throughout the experiment, the value of which was controlled to maintain a target evaporation rate of 0.5% (0.005 ions per pulse).

Reconstruction of the APT data was performed using the Integrated Visualization and Analysis Software package (IVAS) v3.6.6 (CAMECA Scientific Instruments, Madison, WI), and established reconstruction algorithms [54]. For datasets that contained mostly metal, with only fine oxidation along grain boundaries, the profile of the DC voltage during the experiment was assumed to be analogous to the evolution of the tip radius, and the data was reconstructed accordingly. However, for datasets containing large volume fractions of oxide, the differences in evaporation between the oxide and metal phases significantly affect the DC voltage profile. Accurate reconstruction therefore cannot be obtained using the voltage profile for such samples. In these cases, the evolution of the tip radius used for reconstruction was correlated with SEM images of the tip shapes.

3. Results and discussion

3.1. APT and EELS characterization of intergranular oxidation

A SEM image of an internally oxidized Alloy 600 sample is shown in Fig. 1(a). Nodular structures are formed on the surface which, in some cases, line up adjacent to grain boundaries. These topographical features have been previously studied in many classical internal oxidation systems [20–22] with nodules reported to be composed of the solvent metal, in this case Ni. Nodule formation is a result of Ni extrusion driven by the compressive stress generated by the volumetric expansion during internal Cr and/or Fe oxidation [17–19,33,34,38,39]. Langelier et al. have provided evidence that the solvent metal, Ni in Alloy 600, can be transported to the surface via short-circuit oxide-metal interfaces [40]. As seen in Fig. 1(a), alignment of nodule distribution is observed in areas with high dislocation densities, such as minor scratches. Fig. 2(b) shows a cross-section of the Alloy 600 grain boundary in Fig. 1(a). Intergranular oxidation depth is approximately 2 μm; similar penetration depth was consistently observed across all grain boundaries targeted for APT or STEM characterization. Furthermore, comparable intergranular oxidation has been shown to promote embrittlement of grain boundaries in Ni alloys and stainless steels, best demonstrated by the recent micro-mechanical testing of Lozano-Perez et al. [55–57] and Stratulat et al. [58] on oxidized and unaffected grain boundaries.

STEM-EELS results for an oxidized grain boundary are presented in Fig. 3; the boundary exhibits a curved nature. Further EELS mapping of Ni and Cr distributions (Fig. 3(b) and (c), respectively) reveals that,
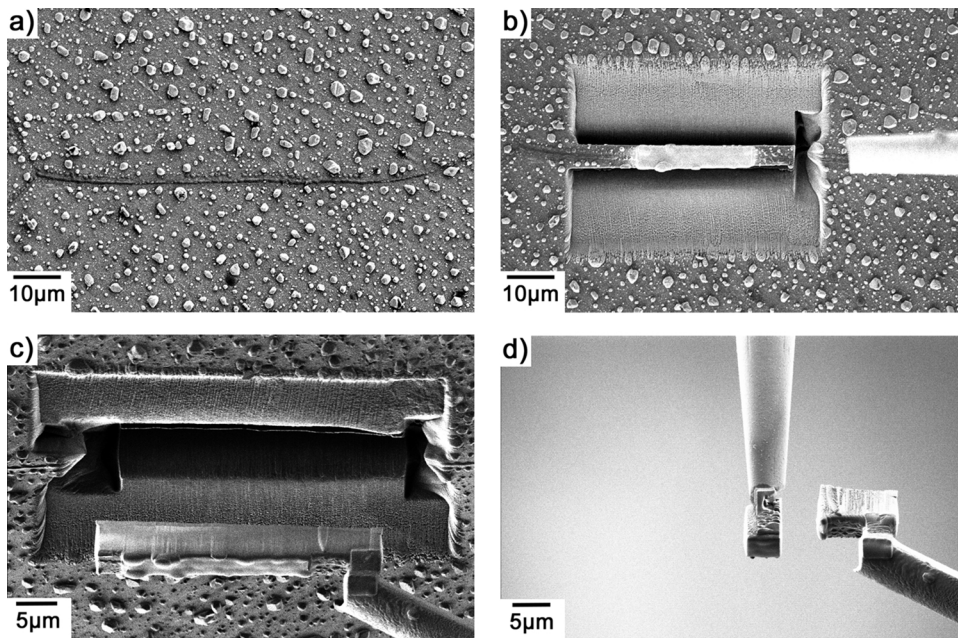
Fig. 1. SEM images of the typical FIB extraction procedure for grain boundary APT samples from Alloy 600. (a) Selection of grain boundary area, (b) milling of sample wedge for extraction, (c) extraction of the wedge, (d) fixing wedge sections onto pre-sharpened needles.
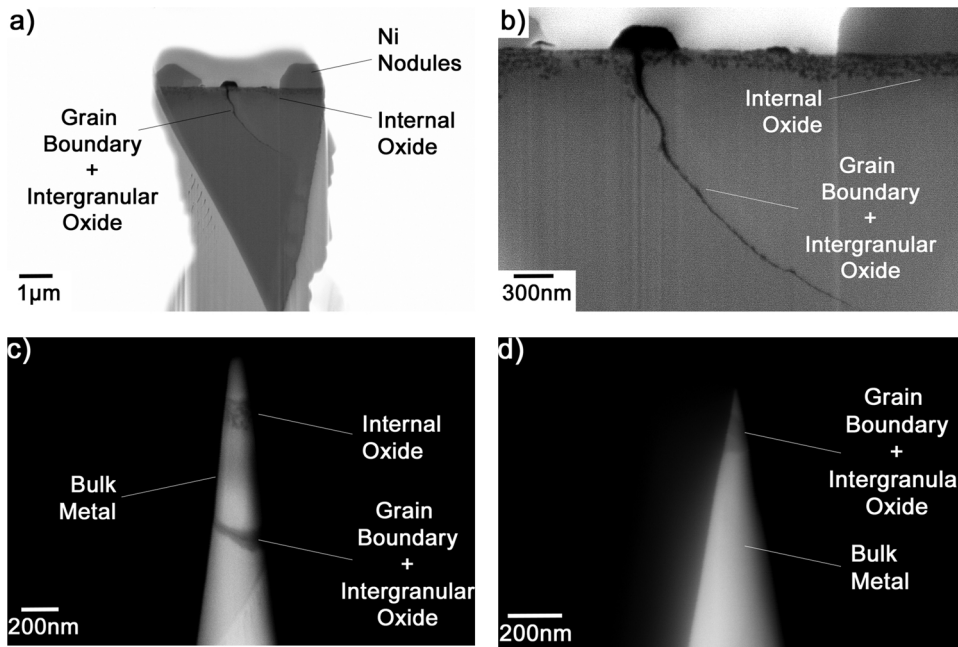
Fig. 2. SEM images of the typical FIB sharpening procedure for preparing APT samples containing oxidized grain boundaries from Alloy 600. (a) examining wedge cross-section to reveal the oxidized boundary, (b) detail of cross-section shown in (a), (c) sample following annular milling, (d) APT sample following final sharpening.

between the curved path of the oxidized boundary and an originally-straight line, are regions of Ni enrichment and Cr depletion. This morphology is indicative of DIGM having occurred in this sample during exposure. The maximum distance of migration away from the original plane of the grain boundary ranges from approximately 300 nm–620 nm. It is also observed that the depth at which DIGM takes place exceeds that of the continuous intergranular oxide by almost 1 μm. EELS concentration maps reveal that O and Cr are segregated at the boundary below the continuous oxidation front, while Ni is depleted. Also, the minor element Ti is found segregated at the boundary, as observed by the EELS map in Fig. 3(d). These findings are consistent with several studies that report that the intergranular oxide(s) formed in solution annealed Alloy 600 exposed to 480 °C hydrogenated steam consist of a mixture of Cr, Ti, and Al oxides [18,34,38–41]. Here it should be noted that the detection of Al was outside the energy window mapped by EELS for the results presented in Fig. 3. Therefore, the

segregation of Al in the intergranular oxide cannot be confirmed by the current STEM-EELS results (although the APT data presented further below demonstrate its presence).

Characterization of the thicker portions of the intergranular oxide by APT frequently resulted in fracture of the specimen, due to the brittle nature of the intergranular oxide. This characteristic of the sample prevented successful APT analysis of an entire oxidized grain boundary near the surface, where the oxide was thickest and most well-developed. APT reconstruction for a sample which included a portion of this well-developed near-surface oxide adjacent to a grain boundary is shown in Fig. 4. However, this reconstruction does not include the centre of the grain boundary oxide itself. The overall composition of the oxide is shown in Table 2, which shows the oxide to be enriched in Cr, with a composition approaching that of Cr_2O_3.

The distribution of major alloying elements and oxygen at the metal-oxide interface is given in Fig. 4(b). Slight Fe enrichment is
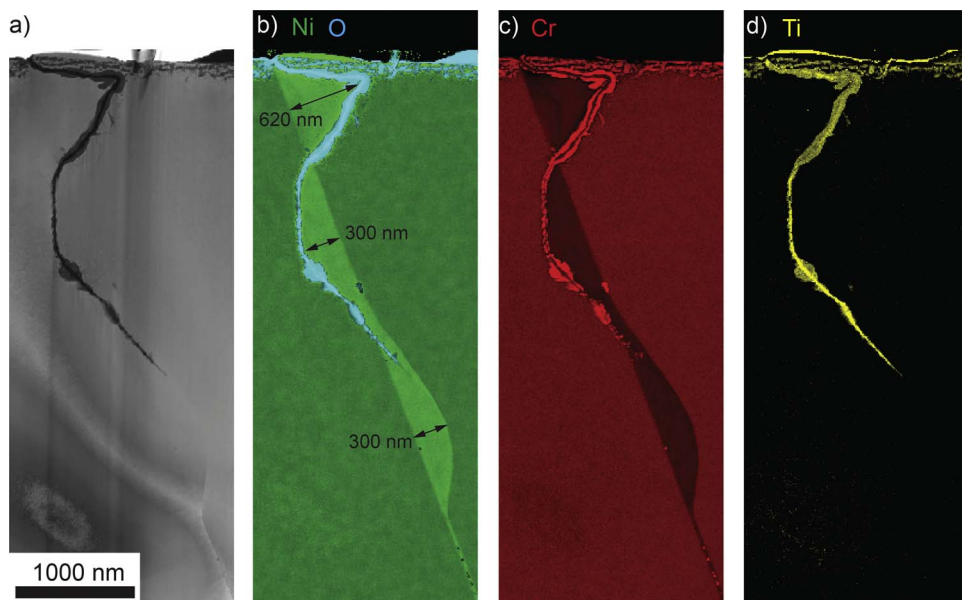
Fig. 3. (a) HAADF-STEM image of an oxidized grain boundary in Alloy 600, and corresponding EELS maps for (b) Ni, O, (c) Cr and (d) Ti. Distances indicating the width of DIGM are included in (b).

apparent at the interface. In addition, Ni is depleted in the intergranular oxide and enriched in the metal directly adjacent to the oxide. Intergranular oxidation has likely resulted in Ni being displaced to the intergranular oxide-metal interface which results in Ni-rich pathways that allow for eventual outward Ni diffusion to the surface, as originally shown by Langelier et al. [40]. Ni expulsion directly on the surface of grain boundaries is not evident in Fig. 1(a), but aligning of nodules near

grain boundaries has been reported previously for internally oxidized Alloy 600 [18,19,37–39]. Inward intergranular oxide growth, initiating at the surface, likely blocks Ni from diffusing directly to the surface of grain boundaries. Instead, outward Ni flow along the intergranular oxide-metal interface may eventually coalesce with Ni pathways formed at internal oxide-metal interfaces in the matrix directly adjacent to the grain boundaries. Minor impurity element distribution at the
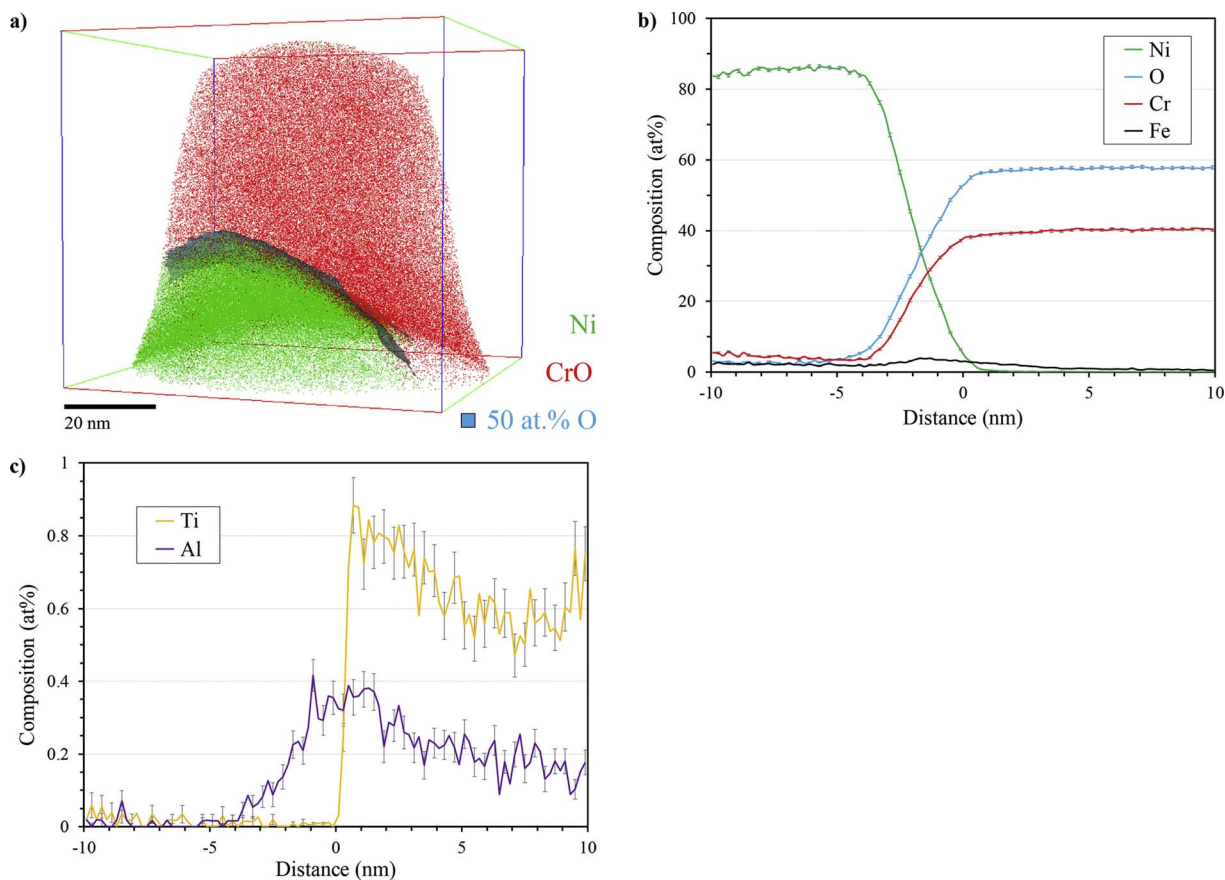
Fig. 4. APT analysis volume containing near-surface grain boundary oxides in Alloy 600. (a) 3D atom map showing Ni, CrO ions, and 50 at.% O isosurface. (b) 2D composition map from a 20 nm thick cross-section, showing Fe concentration. (c, d) proximity histograms (proxigrams) from lower isosurface shown in (a), with 1D concentration profiles plotted for (c) Ni, O, Cr, Fe and (d) Ti, Al.

Table 2
APT measured composition for the grain boundary oxide shown in Fig.4.

Composition (at.%)						
Ni	Cr	Fe	O	Al	Ti	Mn
0.09 ± 0.01	39.7 ± 0.02	0.85 ± 0.01	57.7 ± 0.04	0.18 ± 0.01	0.63 ± 0.01	0.10 ± 0.01
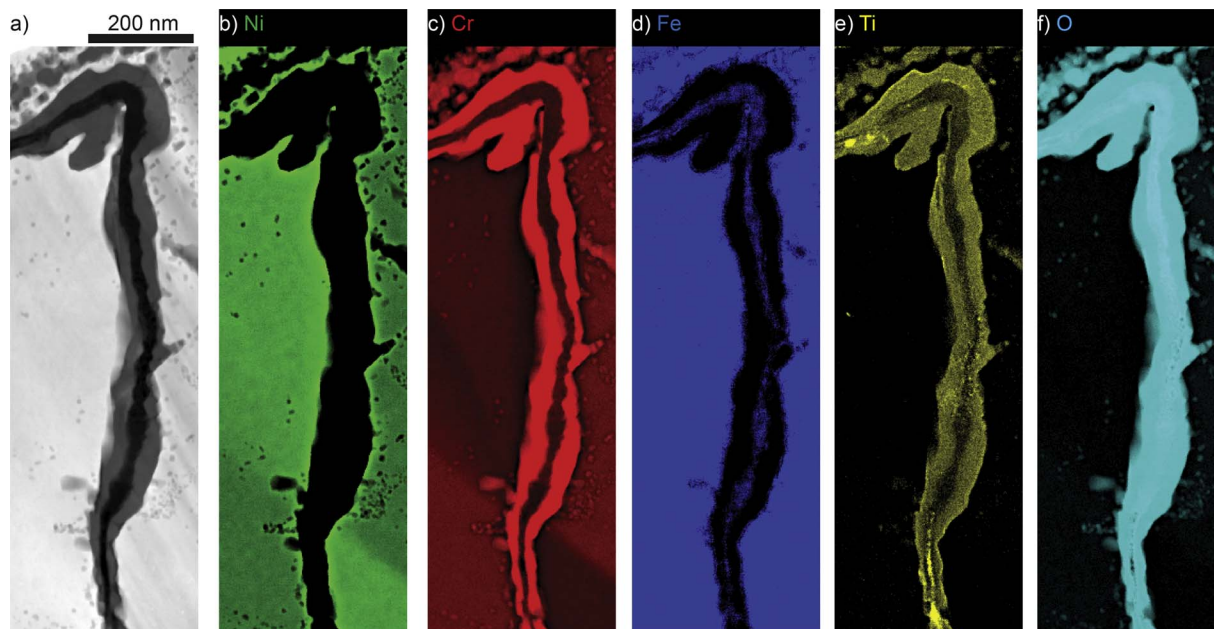
Fig. 5. (a) HAADF-STEM image of the near-surface intergranular oxide, and corresponding EELS maps for (b) Ni, (c) Cr, (d) Fe, (e) Ti, and (f) O.

oxide-metal interface is shown in Fig. 4(c); Ti and Al are observed to segregate to oxidized regions. The minor alloying element contents in the well-developed intergranular oxide, not directly on the grain boundary, is less than 1 at.%, which is reasonable given their contents in Alloy 600, in Table 1. These observations suggest that in the well-developed portion of the intergranular oxide minor impurity elements segregate or oxidize at different interfaces, likely dependent on their relative nobilities, but the overall concentration remains similar to the pristine alloy. Further STEM-EELS maps for the near surface intergranular oxide in Fig. 3(a) are shown in Fig. 5. In addition to Cr and Ti, the near-surface intergranular oxide also contains a significant Fe content. In addition, discrete internal oxide nano-particles are observed in the matrix regions adjacent to the intergranular oxide. The core (centre) grain boundary oxide transitions from an Fe-rich oxide near the sample surface to a Ti-rich oxide with continued intergranular oxide growth. The reason for this oxide chemistry transition is unclear, but may be related to the presumably low concentration of Ti at the grain boundary during early stage oxidation. With increased exposure duration at 480 °C, Ti may have sufficient time to diffuse to grain boundaries, allowing for the eventual formation of thermodynamically favourable Ti-rich oxide(s) at greater oxide penetration depths.

STEM-EELS analysis of a region containing the continuous intergranular oxide front and the area ahead is presented in Fig. 6. Elemental distributions given by EELS maps of Ti, Cr, Ni, and O are generally consistent with observations of the thicker intergranular oxide, nearer the surface, presented in Figs. 4 and 5. It is however notable that at the continuous intergranular oxide front, the composition of the oxide becomes relatively more enriched in Ti than Cr, especially at the core (centre). Also, Fe is heavily depleted in the oxide. APT analysis from a similar region, near the intergranular oxidation front, is given in Fig. 7 for comparison using a technique with superior elemental sensitivity. At this depth, the intergranular oxide is 8–10 nm thick. 1D

composition profiles of the major alloying elements and O, in Fig. 7(b), reveal segregation of Cr to the grain boundary in oxidized regions and accompanying Ni enrichment adjacent to the grain boundary. There is also a depletion of Fe at the boundary. 1D composition profiles for the minor elements are provided in Fig. 7(c), which reveal that Al and Ti are significantly enriched in the intergranular oxide. Previous studies have reported comparable findings for intergranular Al and Ti oxidation in Alloy 600 exposed to similar conditions [18,37–39,41]. Ni enrichment, and corresponding solute element depletion, is observed to occur more favorably on the right side of the grain boundary, as shown in the 1D composition profiles in Fig. 7(b) and (c). Therefore, a greater fraction of the solute oxidized at the boundary has come from the right grain, which is a result consistent with previous reports of DIGM in this alloy [37–39,41,44–47].

Bertali et al. suggested that thermodynamically favourable Al and Ti oxidation may precede Cr-rich oxide formation [37–39] and play a fundamental role in the intergranular oxidation embrittlement of Alloy 600. In agreement with their findings, 3D APT in Fig. 7 reveals that significant Al and Ti oxidation has occurred prior to or concurrent with initial formation of Cr-rich oxide at the grain boundary. Surprisingly, minor alloying elements, Ti and Al, are observed to concentrate from less than 0.5 at.% in the bulk alloy to levels of up to 4 at.%. One possible explanation for this increase could be migration of the grain boundary towards the grain with more favourable diffusion kinetics, which increases the outward diffusive flux of reactive minor alloying elements. This is explored in further detail in Section 3.2.

The APT analysis volume in Fig. 8(a) is taken from an un-oxidized section of a grain boundary, directly ahead of the intergranular oxide. Unlike previous Alloy 600 APT analysis volumes, no oxygen is present at this distance ahead of the grain boundary oxide. Instead, the grain boundary is revealed in the 3D Cr concentration map, shown in Fig. 8(b), because of the difference in Cr concentrations in the bulk
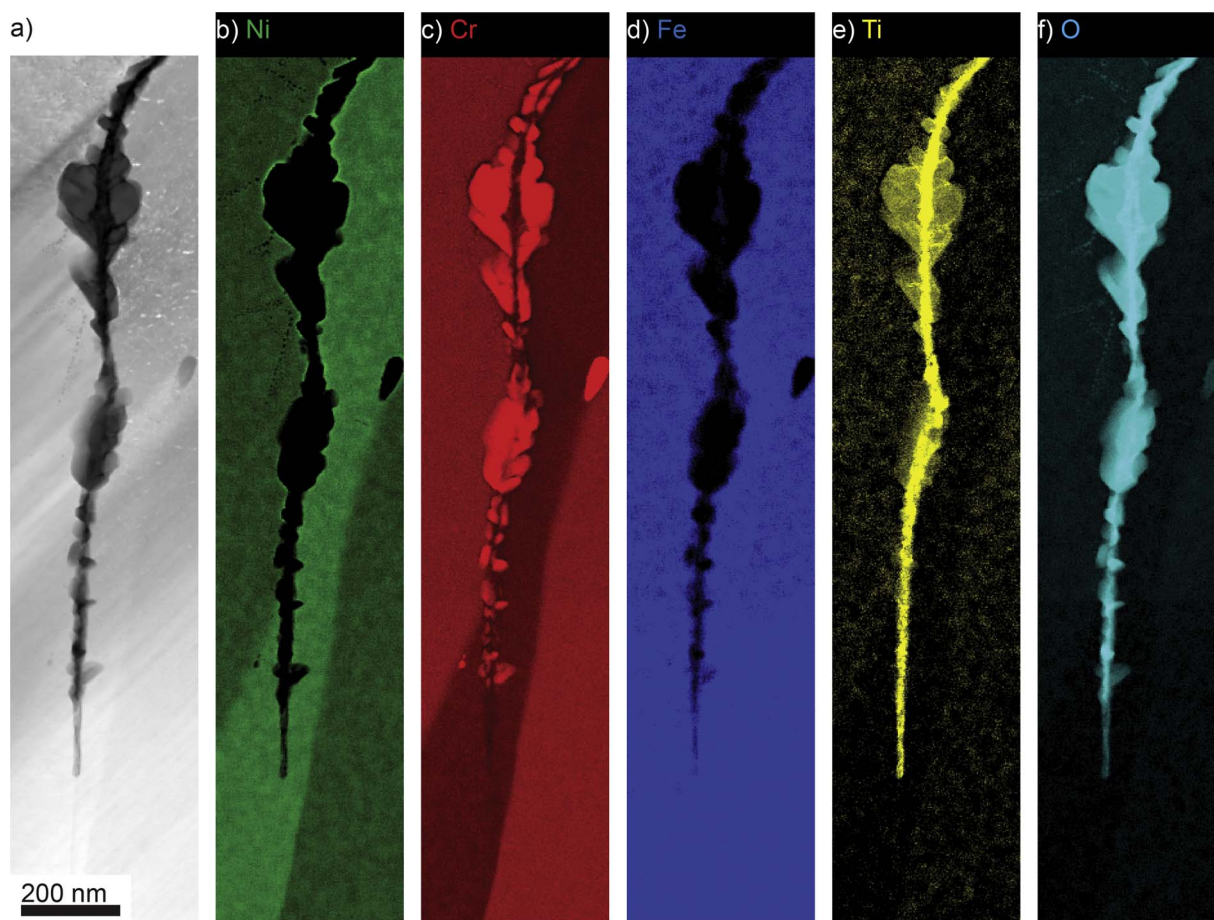
Fig. 6. (a) HAADF-STEM image of the intergranular oxidation front and the area ahead with corresponding EELS maps for (b) Ni, (c) Cr, (d) Fe, (e) Ti, and (f) O.

alloy and the DIGM-affected grain; this decrease in solute Cr content and increase in Ni in the right grain, due to DIGM, is evident in the 1D composition profile in Fig. 8(c). In addition, DIGM has resulted in reactive Ti and Al contents in the DIGM-affected grain dropping significantly. Essentially, reactive elements (Ti, Al, Cr) have been "swept" to the grain boundary in the migrated region and likely diffused upward to the growing intergranular oxide front. Therefore, DIGM may aid in explaining the increased kinetics for outward intergranular Cr diffusion at 480 °C. In addition, the occurrence of DIGM may account for the enrichment of Ti and Al in the intergranular oxide well beyond what would be possible through conventional lattice diffusion. Oxygen diffusion at grain boundaries could also be a driving force for accumulation of solute reactive species; however, even with the high elemental sensitivity of APT, no oxygen could be detected.

3.2. Explaining enhanced transport of Al and Ti

As mentioned previously, the enrichment of Al and Ti at the grain boundaries is surprising given their low bulk contents in Alloy 600 of 0.37 at.% for Ti and 0.34 at.% for Al (see Table 1), particularly considering the presumably low lattice diffusion rates at the temperature of exposure. It is notable that Ti segregation is not observed ahead of the grain boundary migration front in Fig. 1, thus confirming that after a solution anneal the minor elements are not originally concentrated at grain boundaries (i.e prior to exposure). Oxide-metal interfaces and dislocation pipe diffusion may increase the diffusion rate of minor elements to grain boundaries, similar to what has been proposed for the formation of surface Ni nodules [40]; however, these mechanisms are unlikely to provide the total flux of minor elements from the bulk required to achieve the observed Ti and Al enrichment.

We propose that the key factor causing significant minor element segregation is the grain boundary migration caused by diffusion of these species, favorably from one grain. Theoretically, DIGM may assist in explaining the high concentration of minor alloying elements observed to segregate to the grain boundary, assuming a sufficient migration distance is attained. The grain boundary observed in Fig. 3 migrates a significant distance, with this migration zone extending almost a micron ahead of the intergranular oxide front. The grain boundary is observed to migrate a maximum distance of 620 nm near the surface, and 300 nm deeper into the material, with an average DIGM distance within the material of approximately 122 nm. By using these distances to estimate the composition change in the volume of migrated material, an approximation of the theoretical minor element segregation at the boundary can be achieved, assuming complete "sweeping" of the minor elements to the grain boundaries by DIGM.

The number of atoms for a given solute, i, which are removed from solution and segregated to the grain boundary via DIGM ($n_{i,m}$) may be expressed using the following equation, which considers the volume of material passed by the migrating boundary:

$$n_{i,m} = (X_0 - X_m)\rho V_m \tag{1}$$

where X_0 and X_m are the atomic fractions of the solute i in the original and migrated grains, respectively, ρ is the atomic density of the grains, and V_m is the volume of the migrated region of the grain. If we assume that in the current Alloy 600 samples, intergranular oxidation and boundary migration will be relatively uniform along the length of the grain boundary, we may consider the case of a slice of material of unit thickness, t, such that $V_m = A_m t$, where A_m is the migrated area.

For DIGM to be the dominant mechanism by which the significant segregation of minor alloying elements occurs, the total solute atoms
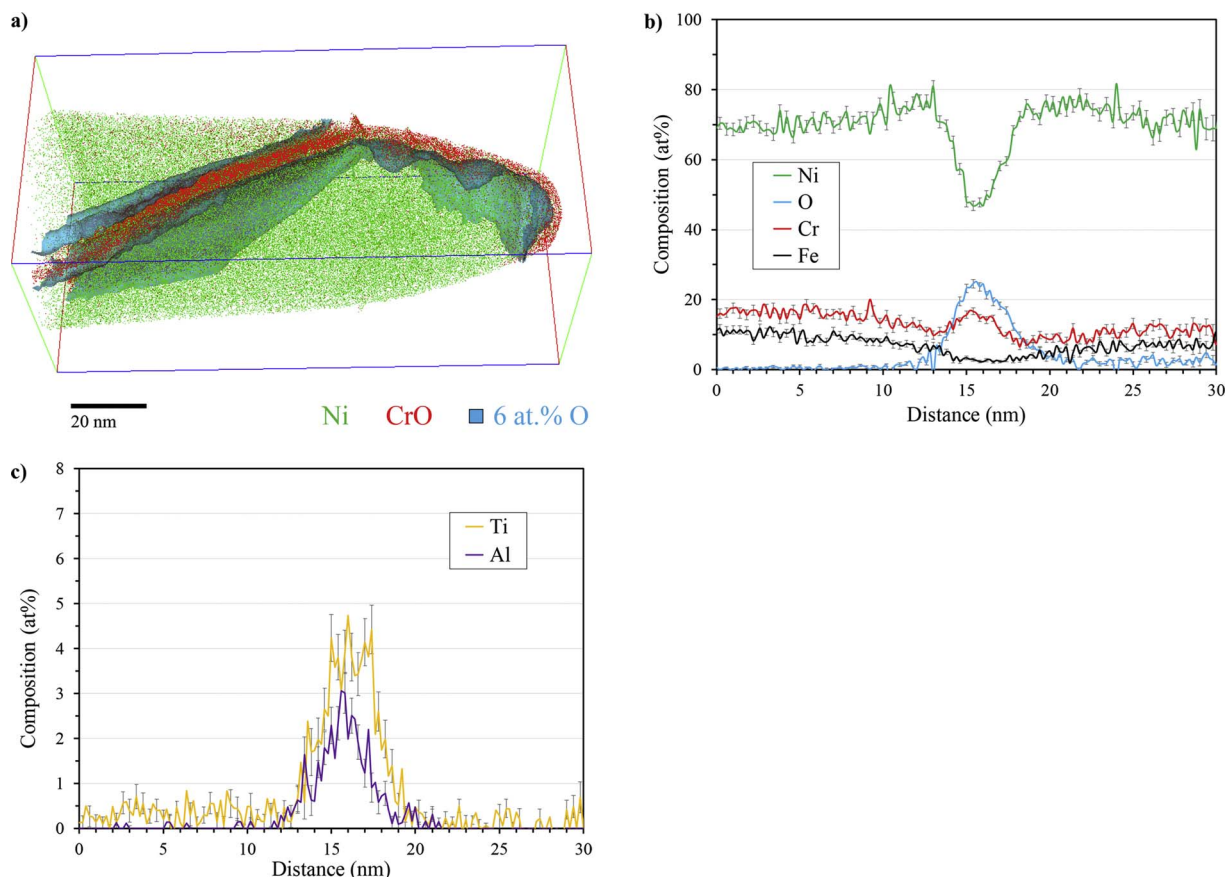
Fig. 7. Analysis of an APT volume containing an oxidized grain boundary in Alloy 600 near the intergranular oxidation front. (a) 3D atom map showing Ni, CrO ions, and 6 at.% O isosurface. 1D concentration profiles normal to the grain boundary are provided for (b) Ni, O, Cr, Fe, and (c) Ti, Al.

passed by the boundary should be equal to the amount of segregated solute atoms. The solute atoms segregated per unit area of the grain boundary can be calculated using APT results, by taking a sub-volume running normal to the boundary, and integrating the solutes. The total segregated solutes ($n_{i,s}$) can then be estimated by using the length of the oxidation along the migrated boundary (L) for a unit thickness, as related by the following equation:

$$n_{i,s} = \frac{\sum n_i}{\eta A_0} Lt \tag{2}$$

where $\sum n_i$ is the sum of solute atoms measured by integration of a one-dimensional APT profile through the sub-volume, A_0 is the cross-sectional area of that sub-volume, and η is the detection efficiency of the atom probe.

To check if Eqs. (1) and (2) produce equivalent values, experimental data can be input from the STEM-EELS and APT results of this work. Using APT measurements for Ti and Al, the length of oxidation can be calculated based on the migrated area observed in Fig. 3. The calculated values for this length are plotted in Fig. 9, and compared to the measured value from Fig. 3. The calculated result is in good agreement with the observed distance for oxide growth in Alloy 600, as presented in Fig. 3, given the method of approximation, variability in minor element content along the grain boundary from EELS, and how various factors are not accounted for, (e.g. other sources of short-circuit diffusion). The good agreement supports the idea of DIGM as a process that can account for the enhanced intergranular concentrations of minor alloying elements, on the scale of the values observed in this work. A similar calculation could be done for Cr to determine the effect of DIGM on intergranular Cr diffusion, and possibly estimate the total volume of oxide, but is beyond the scope of the present work. A recent publication by the authors further investigates DIGM effects on Cr oxidation, the

influence of intergranular Cr carbide precipitation, and how grain boundary migration may affect the SCC susceptibility of Alloy 600 of different heat treatments [41].

Several studies have reported significant Al and Ti intergranular oxidation in Alloy 600 exposed to high temperature hydrogenated steam [18,37–39,41]. The high concentration of minor impurities at the grain boundaries was very surprising, given the hindered kinetics in the exposure conditions, but results of the present study strongly suggests DIGM as a viable explanation. In accordance with Bertali et al., thermodynamically favourable intergranular Ti and Al oxidation is observed to occur prior to Cr-rich oxide formation in the continuous intergranular oxide which extends downward from the surface of Alloy 600 [37]; the formation of Cr, Ti, and/or Al-rich discrete internal oxide precipitates may precede both of these processes and is discussed further in Section 3.3. The presence of initial Ti and Al oxides may provide additional short-circuit diffusion paths for oxygen and/or Ni along oxide-metal interfaces. However, these results should be considered specific to solution annealed (∼1050 °C) Alloy 600 (i.e. dissolution of carbides and homogeneity in bulk composition). In mill annealed Alloy 600 Ti may form precipitates with C and/or N which remove the element from the matrix. In thermally treated Alloy 600, intergranular Ti and Al oxidation has been demonstrated in previous studies [18,39,41], likely a result of competing Cr carbide precipitation which allows for significant Ti remaining in the matrix. Also, in the absence of minor alloying element oxidation, embrittlement of Alloy 600 likely still occurs due to intergranular Cr oxidation, which generates compressive stress and weakens bonding at the grain boundaries. Therefore, whether minor alloying element oxidation plays a fundamental role in an intergranular oxidation embrittlement SCC mechanism remains uncertain.
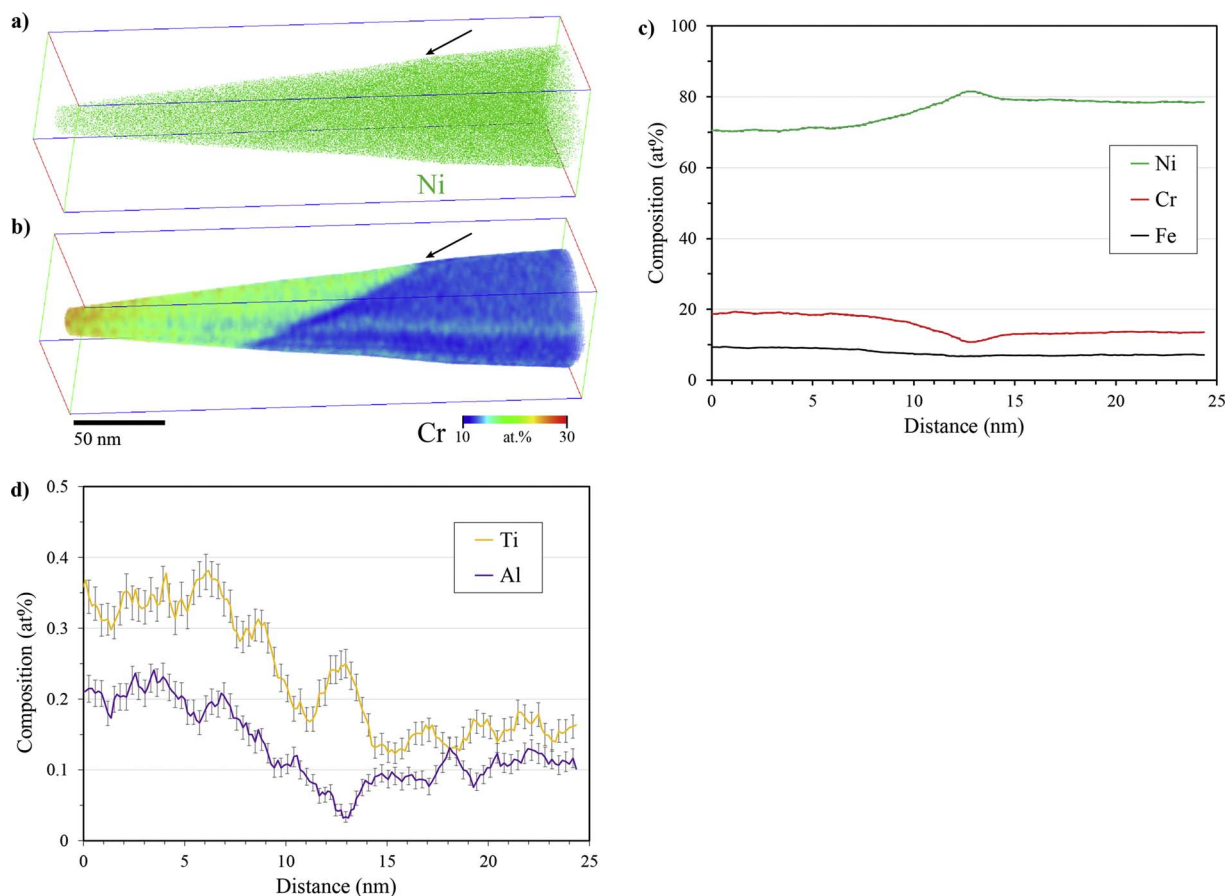
Fig. 8. APT analysis volume of a grain boundary in Alloy 600 just ahead (< 1 μm) of the intergranular oxidation front. (a) 3D atom map showing Ni ions, (b) 3D Cr relative concentration temperature map, (c,d) 1D concentration profiles normal to the grain boundary, for (c) Ni, Cr, Fe, and (d) Ti, Al. The grain boundary is indicated by arrows in (a) and (b) based on Cr depletion and/or Ni enrichment.
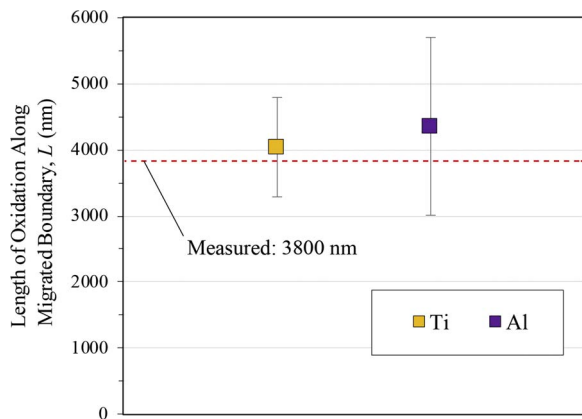
Fig. 9. Calculated versus measured length of oxidation along the migrated boundary in Fig. 3 using equations (1) and (2) for Ti and Al.

3.3. Evidence of an initial internal oxidation process

In the current work, conditions are maintained at an oxygen partial pressure well below the equilibrium Ni/NiO dissociation pressure. In Alloy 600, the reactive alloying element contents (Fe, Cr, Ti, Al, etc.) are not high enough to allow for external oxidation below 500 °C; instead, two alternate oxidation processes are often referenced as plausible in hydrogenated steam or water below 500 °C: continuous preferential intergranular oxidation of reactive alloying elements extending downward from the surface, and/or internal oxidation whereby oxygen diffuses into the metal, at grain boundaries or in the

matrix, forming discrete oxide particles with reactive alloying elements. In Fig. 3, preferential intergranular oxidation of Ti and Cr is observed to extend downward from the surface, with the existence of undetected Al oxide suggested by the APT data; however, discrete internal oxide particles are also observed to form approximately 1 μm ahead of the continuous intergranular oxide front.

Fig. 10 shows high resolution EELS elemental maps for the discrete internal oxide precipitates, present well ahead of the preferential intergranular oxide front. No C was detected in the EELS spectra, confirming that these are not Ti or Cr carbide phases. Slight Ti enrichment is observed in the centre of the particles, providing further support for impurity element oxidation, Ti and/or Al, prior to Cr oxide formation. The presence of discrete oxide particles provides evidence that intergranular internal oxidation is possible in Alloy 600 after exposure to 480 °C hydrogenated steam. Intragranular internal oxidation has been previously demonstrated in Alloy 600 and other Ni alloys in both 480 °C hydrogenated steam and high temperature water [15–18,33,34,37–40,42–44]; however, only continuous preferential oxidation had been reported at grain boundaries. The absence of prior evidence for intergranular internal oxidation in Alloy 600 in high temperature steam is likely linked to lack of analysis well ahead of the connected intergranular oxide front and possible three-dimensional changes missed by extraction of only a few TEM samples; the importance of accounting for three-dimensional changes during intergranular oxidation of Alloy 600 has recently been demonstrated by Langelier et al. [41] using a 3D FIB serial sectioning technique. Alternatively, internal oxide precipitates may eventually coalesce with continued growth and form a connected intergranular oxide leading to the appearance of exclusive preferential intergranular oxidation in
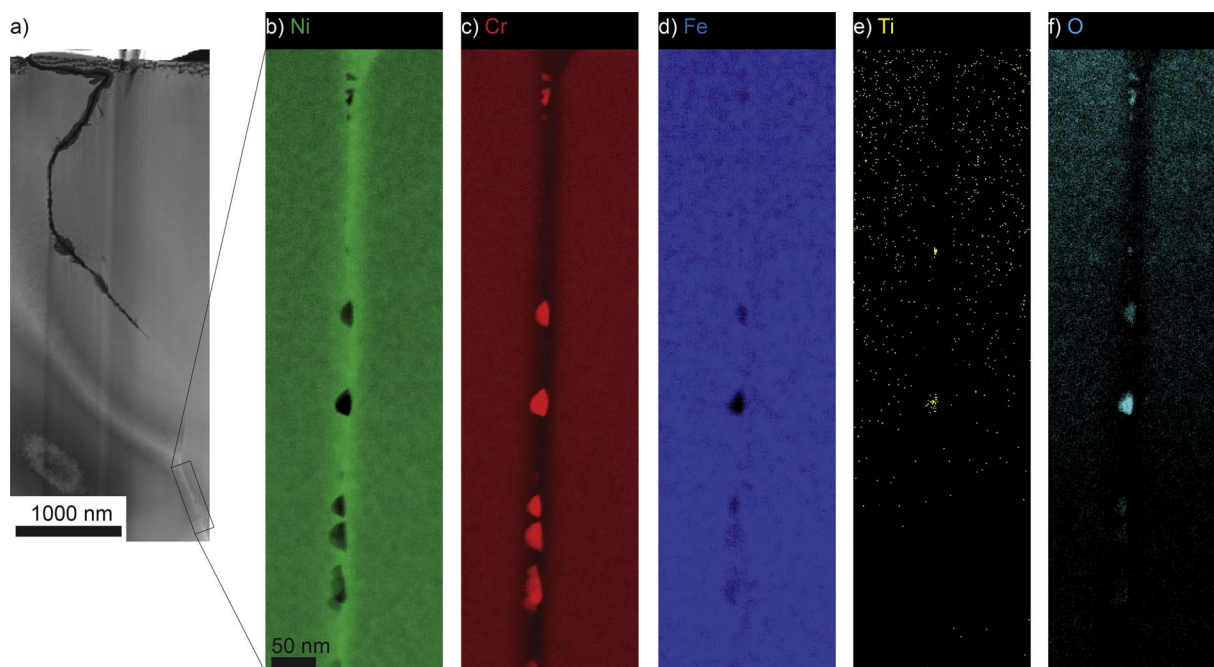
Fig. 10. (a) HAADF-STEM image showing the location of discrete intergranular internal oxide particles ahead of the migration front, with EELS elemental maps for (b) Ni, (c) Cr, (d) Fe, (e) Ti, and (f) O.

Alloy 600.

Results of the current study suggest that a combination of preferential intergranular oxidation and internal oxidation are possible intergranularly in Alloy 600 exposed to 480 °C hydrogenated steam. Intergranular internal oxidation is usually studied at temperatures greater than 600 °C, but is now shown to extend to lower temperatures. However, "low" temperature internal oxidation differs in terms of relative scale when compared to classical internal oxidation systems. Hindered kinetics at lower temperature results in the discrete internal oxide particles forming only a few nanometers apart, as a consequence of the expected slower oxygen diffusion kinetics. Also, the internally oxidized zone (IOZ) is greatly reduced in terms of penetration depth at temperatures less than 500 °C.

In the present study, the intergranular oxide may be formed through initial preferential oxidation down from the surface causing the area ahead of the intergranular oxidation front to eventually become Cr, Al, and Ti depleted, and Ni-rich, as a result of DIGM (see Fig. 8). Therefore, further oxidation may not be favourable in this non-reactive Ni-rich area. Instead, oxygen may diffuse to the undisturbed boundary well ahead of the Ni-rich region (at the grain boundary migration front) where reactive element (Cr, Ti, Al, etc.) concentrations can support further oxidation as discrete particles, as observed in Fig. 3. Eventually, the combined reactive element flux from grain boundary migration and intergranular diffusion may grow the discrete internal oxide precipitates until they coalesce and join with the intergranular oxide front. Alternatively, intergranular internal oxidation of Alloy 600 may precede the formation of the continuous intergranular oxide extending down from the surface – i.e. discrete internal oxides are formed initially and then connected as Cr diffuses to the grain boundary. Such a process is likely accelerated through extensive grain boundary migration and other short-circuits. Further work is required to better understand the mechanism of discrete intergranular internal oxide formation in Alloy 600 and other alloys containing low reactive solute element contents at low temperatures where lattice diffusion is negligible.

Scott and Le Calvar originally proposed internal oxidation as the mechanism of SCC in Alloy 600 exposed to 300 °C–360 °C water with added H$_2$ [6]. Several studies have since indicated that primary water conditions, in the vicinity of the Ni/NiO equilibrium electrode potential, can produce preferential intergranular oxidation embrittlement through a process analogous to internal oxidation [23–29]; the oxidation occurs for similar reasons as internal oxidation at higher temperatures, but kinetic limitations result in discrete particle formation either being more subtle or not occurring at all. Similar intergranular phenomena are observed in Alloy 600 exposed to high temperature hydrogenated steam and representative primary water: preferential intergranular oxidation (including chemistry), Ni enrichment ahead of the intergranular oxide, and grain boundary migration [17–19,30–38]. Although lattice diffusion is essentially negligible in both environments, the magnitude of each of the aforementioned processes is limited in high temperature water compared to hydrogenated steam due to further diffusion kinetic limitations. Therefore, while the use of high temperature steam as an accelerated simulant of primary water is valid based on the work of Economy et al. [36] and experimental observation, it should be noted that 480 °C hydrogenated steam produces accelerated conditions resulting in enhanced kinetics for processes that are often subtler in representative primary water, such as grain boundary migration, minor alloying element diffusion, inward oxygen diffusion, and intergranular oxide penetration. Readers are referred to a recent review article [59] for further discussion on the validity of hydrogenated steam at less than 500 °C as a representative environment for primary water.

In addition to reducing the magnitude of observed phenomena, the hindered diffusion kinetics in high temperature water could also result in some experimental observations in 480 °C hydrogenated steam not extending to lower temperatures. For example, the formation of discrete internal oxides ahead of the continuous intergranular oxide, observed in the current study, has never been observed in 300 °C–360 °C water to the magnitude observed here; although, the idea of discrete intergranular internal oxides as a precursor to the often reported continuous preferential intergranular oxide has been put forth several times by Scott and others [6,23,25]. It is possible that internal oxidation does not occur in Alloy 600 when the temperature is extended down to 300 °C due to kinetic limitations; however, studies investigating this possibility have thus far been limited. Therefore, given the known similarities between the two environments, the possibility of intergranular internal oxidation in Alloy 600 exposed to 300 °C to 360 °C water should not be

overlooked; further studies should be performed to evaluate whether formation of discrete nano-scale internal oxide particles is possible well ahead of the intergranular oxide front in Alloy 600 exposed to high temperature water.

4. Conclusions

Initial intergranular oxidation processes in Alloy 600 exposed to 480 °C hydrogenated steam have been examined on a nano-scale by STEM-EELS and APT. Specifically, minor element oxidation, DIGM, and the possibility of intergranular internal oxidation were explored. The complementary TEM and APT characterization techniques employed have provided new insights into sub-nanometre scale mechanisms by which initial intergranular oxidation occurs at low temperature in Alloy 600.

- Continuous preferential intergranular oxidation in Alloy 600 is observed after exposure to 480 °C hydrogenated steam. APT results revealed that Ti and/or Al oxides are formed initially and later surrounded by a Cr-rich oxide.
- Extensive grain boundary migration is observed along and ahead of the intergranular oxide formed in Alloy 600. Reactive elements, Cr, Al, and Ti, are observed to segregate to the grain boundary while migrated regions are enriched in Ni.
- Intergranular concentrations of the minor elements, Ti and Al, far exceed their bulk values. It is suggested that DIGM causes this large-scale segregation of minor elements. This is supported by calculations showing that the amount of Ti and Al enriched oxide is in good agreement with the amount removed from the migrated volume.
- Discrete oxide particles are formed well ahead of the intergranular oxide front, suggesting that intergranular internal oxidation is possible in Alloy 600 exposed at 'low' temperature in 480 °C hydrogenated steam.
- Given the known similarities between intergranular oxidation phenomena in Alloy 600 extending from reducing 300 °C water to 500 °C steam, the possibility of small-scale intergranular internal oxidation should be further investigated in representative primary water conditions.

Acknowledgements

References

[1] D.S. Morton, S.A. Attanasio, G.A. Young, P.L. Andresen, T.M. Angeliu, The influence of dissolved hydrogen on nickel alloy SCC: a window to fundamental insight, NACE Corrosion, NACE International, 2001 Paper No. 01117.
[2] D.S. Morton, S.A. Attanasio, E. Richey, G.A. Young, In search of the true temperature and stress intensity factor dependencies for PWSCC, in: T.R. Allen, L. Nelson, P.J. King (Eds.), Proc. 12th Int. Conf. on Environmental Degradation of Materials in Nuclear Power Systems–Water Reactors, The Minerals, Metals, and Materials Society [TMS], Salt Lake City, UT, 2005, pp. 977–988.
[3] D.S. Morton, S.A. Attanasio, G.A. Young, Primary Water SCC Understanding and Characterization Through Fundamental Testing in the Vicinity of the Nickel/Nickel Oxide Phase Transition, (2002) Schenectady, NY.
[4] P.L. Andresen, J. Hickling, K.S. Ahluwalia, J. Wilson, Corrosion 64 (2008) 707–720.
[5] P.L. Andresen, J. Hickling, A. Ahluwalia, J. Wilson, Effect of dissolved hydrogen on SCC of Ni alloys and weld metals, NACE Corrosion, Paper No. 09414, NACE International, Atlanta, GA, 2009.
[6] P.M. Scott, M. Le Calvar, Some possible mechanisms of intergranular stress corrosion cracking of alloy 600 in PWR primary water, in: E.P. Simonen (Ed.), Proc. 6th Int. Conf. on Environmental Degradation of Materials in Nuclear Power Systems–Water Reactors, The Minerals, Metals, and Materials Society [TMS], San Diego, CA, 1993, pp. 657–665.
[7] L. Bradley, G.C. Wood, F.H. Stott, Mater. Sci. Forum 251–254 (1997) 341–348.
[8] H.C. Yi, S.W. Guan, W.W. Smeltzer, A. Petric, Acta Metall. Mater. 42 (1994) 981–990.
[9] G. Gulsoy, G.S. Was, Metall. Mater. Trans. A 46 (2015) 525–535.
[10] F.H. Stott, Y. Shida, D.P. Whittle, G.C. Wood, Oxid. Met. 18 (1982) 127–146.
[11] F.H. Stott, G.C. Wood, Mater. Sci. Technol. 4 (1988) 1072–1078.
[12] Y. Niu, X.J. Zhang, Y. Wu, F. Gesmundo, Corros. Sci. 48 (2006) 4020–4036.
[13] D.P. Whittle, Y. Shida, G.C. Wood, F.H. Stott, B.D. Bastow, Philos. Mag. A 46 (1982) 931–949.
[14] H. Hindam, D.P. Whittle, J. Mater. Sci. 18 (1983) 1389–1404.
[15] S.Y. Persaud, S. Ramamurthy, R.C. Newman, Corros. Sci. 90 (2015) 606–613.
[16] S.Y. Persaud, S. Ramamurthy, R.C. Newman, Corros. Sci. 91 (2015) 58–67.
[17] S.Y. Persaud, R.C. Newman, A.G. Carcea, G.A. Botton, J. Huang, A. Korinek, S. Ramamurthy, Grain boundary embrittlement of alloy 600 by internal oxidation in simulated primary water environments, in: G.O. Ilevbare, P.L. Andresen, M.D. Wright (Eds.), Proc. 16th Int. Conf. on Environmental Degradation of Materials in Nuclear Power Systems–Water Reactors, Omnipress, NACE International Asheville, NC, 2013.
[18] S.Y. Persaud, A. Korinek, J. Huang, G.A. Botton, R.C. Newman, Corros. Sci. 86 (2014) 108–122.
[19] F. Scenini, R.C. Newman, R.A. Cottis, R.J. Jacko, Alloy oxidation studies related to PWSCC, in: P. Allen, L. Nelson (Eds.), Proc. 12th Int. Conf. on Environmental Degradation of Materials in Nuclear Power Systems–Water Reactors, The Minerals, Metals, & Materials Society [TMS], Salt Lake City, UT, 2005, pp. 891–902.
[20] S. Guruswamy, S.M. Park, J.P. Hirth, R.A. Rapp, Oxid. Met. 26 (1986) 77–100.
[21] J.R. Mackert, R.D. Ringle, C.W. Fairhurst, J. Dent. Res. 62 (1983) 1229–1235.
[22] R.A. Rapp, Acta Metall. 9 (1961) 730–741.
[23] L.E. Thomas, S.M. Bruemmer, Corrosion 56 (2000) 572–587.
[24] S. Lozano-Perez, J.M. Titchmarsh, Mater. High Temp. 20 (2003) 573–579.
[25] M. Sennour, P. Laghoutaris, C. Guerre, R. Molins, J. Nucl. Mater. 393 (2009) 254–266.
[26] J. Panter, B. Viguier, J.-M. Cloué, M. Foucault, P. Combrade, E. Andrieu, J. Nucl. Mater. 348 (2006) 213–221.
[27] S. Lozano-perez, M. Meisnar, J. Dohr, K. Kruska, Reviewing the internal oxidation mechanism as a plausible explanation for SCC in PWR primary water, in: P.L. Ilevbare, M.D. Wright (Eds.), Proc. 16th Int. Conf. on Environmental Degradation of Materials in Nuclear Power Systems–Water Reactors, Omnipress, NACE International Asheville, NC, 2013.
[28] S. Lozano-Perez, P. Rodrigo, L.C. Gontard, J. Nucl. Mater. 408 (2011) 289–295.
[29] S.Y. Persaud, J. Smith, A. Korinek, G.A. Botton, R.C. Newman, Corros. Sci. 106 (2016) 236–248.
[30] T.S. Gendron, S.J. Bushby, R.D. Cleland, R.C. Newman, Oxidation embrittlement of alloy 600 in hydrogenated steam at 400 °C, in: T. Magnin (Ed.), Proc. Of the 2nd Int. Conf. on Corrosion-Deformation Interactions, NACE International, Nice, France, 1996, pp. 484–495.
[31] T.S. Gendron, S.J. Bushby, R.D. Cleland, R.C. Newman, Analusis Mag. 25 (1997) 24–28.
[32] R.C. Newman, T.S. Gendron, P.M. Scott, Internal oxidation and embrittlement of alloy 600, in: S.M. Ford, G.S. Was (Eds.), Proc. 9th Int. Conf. on Environmental Degradation of Materials in Nuclear Power Systems–Water Reactors, The Minerals, Metals, and Materials Society [TMS], Newport Beach, CA, 1999, pp. 79–93.
[33] L. Lindsay, F. Scenini, X. Zhou, G. Bertali, R.A. Cottis, M.G. Burke, F. Carrette, F. Vaillant, Characterisation of stress corrosion cracking and internal oxidation of alloy 600 in high temperature hydrogenated steam, in: P.L. Ilevbare, M.D. Wright (Eds.), Proc. 16th Int. Conf. on Environmental Degradation of Materials in Nuclear Power Systems–Water Reactors, Omnipress, NACE International Asheville, NC, 2013.
[34] G. Bertali, F. Scenini, J. Lindsay, B. Winiarski, L. Zhong, M.G. Burke, Oxidation studies of alloy 600 in low pressure hydrogenated steam, in: G.O. Ilevbare, P.L. Andresen, M.D. Wright (Eds.), Proc. 16th Int. Conf. on Environmental Degradation of Materials in Nuclear Power Systems–Water Reactors, Omnipress, NACE International Asheville, NC, 2013.
[35] F. Scenini, R.C. Newman, R.A. Cottis, R.J. Jacko, Corrosion 64 (2008) 824–835.
[36] G. Economy, R.J. Jacko, F.W. Perment, Corrosion 43 (1987) 727–734.
[37] G. Bertali, F. Scenini, M.G. Burke, Corros. Sci. 111 (2016) 494–507.
[38] G. Bertali, F. Scenini, M.G. Burke, Corros. Sci. 100 (2015) 474–483.
[39] G. Bertali, F. Scenini, M.G. Burke, Corros. Sci. 114 (2017) 112–122.
[40] B. Langelier, S.Y. Persaud, R.C. Newman, G.A. Botton, Acta Mater. 109 (2016) 55–68.
[41] B. Langelier, S.Y. Persaud, A. Korinek, T. Casagrande, R.C. Newman, G.A. Botton, Acta Mater. 131 (2017) 280–295.
[42] S.Y. Persaud, S. Ramamurthy, A. Korinek, G.A. Botton, R.C. Newman, Corros. Sci. 106 (2016) 117–126.
[43] M.J. Olszta, D.K. Schreiber, L.E. Thomas, S.M. Bruemmer, Penetrative internal oxidation from alloy 690 surfaces and stress corrosion crack walls during exposure to PWR primary water, in: G. Busby, P.L. Andresen (Eds.), Proc. 15th Int. Conf. on Environmental Degradation of Materials in Nuclear Power Systems–Water Reactors, The Minerals, Metals, & Materials Society [TMS], Colorado Springs, CO, 2011, pp.

331–342.

[44] M.J. Olszta, D.K. Schreiber, M.B. Toloczko, S.M. Bruemmer, Alloy 690 surface na-nostructures during exposure to PWR primary water and potential influence on stress corrosion crack initiation, in: G.O. Ilevbare, P.L. Andresen, M.D. Wright (Eds.), Proc. 16th Int. Conf. on Environmental Degradation of Materials in Nuclear Power Systems–Water Reactors, Omnipress, NACE International Asheville, NC,, 2013.

[45] D.K. Schreiber, M.J. Olszta, L.E. Thomas, S.M. Bruemmer, Grain boundary char-acterization of alloy 600 prior to and after corrosion by atom probe tomography and transmission electron microscopy, in: G.O. Ilevbare, P.L. Andresen, M.D. Wright (Eds.), Proc. 16th Int. Conf. on Environmental Degradation of Materials in Nuclear Power Systems–Water Reactors, Omnipress, NACE International Asheville, NC, 2013.

[46] D.K. Schreiber, M.J. Olszta, D.W. Saxey, K. Kruska, K.L. Moore, S.M. Bruemmer, Microsc. Microanal. 19 (2013) 676–687.

[47] D.K. Schreiber, M.J. Olszta, S.M. Bruemmer, Scr. Mater. 69 (2013) 509–512.

[48] Y.M. Chen, T. Ohkubo, M. Kodzuka, K. Morita, K. Hono, Scr. Mater. 61 (2009) 693–696.

[49] K. Hono, T. Ohkubo, Y.M. Chen, M. Kodzuka, K. Oh-ishi, H. Sepehri-Amin, F. Lia,

T. Kinno, S. Tomiya, Y. Kanitani, Ultramicroscopy 111 (2011) 576–583.

[50] Y.M. Chen, T. Ohkubo, K. Hono, Ultramicroscopy 111 (2011) 562–566.

[51] E.A. Marquis, N.A. Yahya, D.J. Larson, M.K. Miller, R.I. Todd, Mater. Today 13 (2010) 34–36.

[52] C. Oberdorfer, P. Stender, C. Reinke, G. Schmitz, Microscopy and microanalysis, Off. J. Microsc. Soc. Am. 13 (2007) 342–346 Microbeam Analysis Society, Microscopical Society of Canada.

[53] K. Thompson, D. Lawrence, D.J. Larson, J.D. Olson, T.F. Kelly, B. Gorman, Ultramicroscopy 107 (2007) 131–139.

[54] B. Gault, M.P. Moody, J.M. Cairney, S.P. Ringer, Atom Probe Microscopy, Springer Science, New York, 2012.

[55] J. Dohr, D.E.J. Armstrong, E. Tarleton, T. Couvant, S. Lozano-perez, Thin Solid Films 632 (2017) 17–22.

[56] S. Lozano-perez, J. Dohr, M. Meisnar, K. Kruska, Metall. Mater. Trans. E 1A (2014) 194–210.

[57] H. Dugdale, D.E.J. Armstrong, E. Tarleton, S.G. Roberts, S. Lozano-perez, Acta Mater. 61 (2013) 4707–4713.

[58] A. Stratulat, D.E.J. Armstrong, S.G. Roberts, Corros. Sci. 104 (2016) 9–16.

[59] S.Y. Persaud, R.C. Newman, Corrosion 72 (2016) 881–896.